Version of Record: https://www.sciencedirect.com/science/article/pii/S2095927321007210
Manuscript_00f45e887e7d79ee3238da0ab9cfd0dc

Structure design enables stable anionic and cationic redox chemistry in a T2-type Li-excess layered oxide cathode

Xin Cao [a,d,1], Haifeng Li [b,1], Yu Qiao[a,*], Min Jia[a], Hirokazu Kitaura[a], Jianan Zhang[e], Ping He[c], Jordi Cabana[b], Haoshen Zhou[a,c,*]

[a]Energy Technology Research Institute, National Institute of Advanced Industrial Science and Technology (AIST), Tsukuba 305-8568, Japan

[b]Department of Chemistry, University of Illinois at Chicago, Chicago, IL60607, USA

[c]Center of Energy Storage Materials & Technology, College of Engineering and Applied Sciences, Jiangsu Key Laboratory of Artificial Functional Materials, National Laboratory of Solid State Microstructures, and Collaborative Innovation Center of Advanced Microstructures, Nanjing University, Nanjing 210093, China

[d]Graduate School of System and Information Engineering, University of Tsukuba, Tsukuba 305-8573, Japan

[e]College of Materials Science and Engineering, Zhengzhou University, Zhengzhou 450001, China

[1]These authors contributed equally to this work.

E-mail: yuqiao@xmu.edu.cn (Y. Q.); hszhou@nju.edu.cn (H. Z.)

© 2021 published by Elsevier. This manuscript is made available under the Elsevier user license
https://www.elsevier.com/open-access/userlicense/1.0/

Abstract

Coupled with anionic and cationic redox chemistry, Li-rich/excess cathode materials are prospective high-energy-density candidates for the next-generation Li-ion batteries. However, irreversible lattice oxygen loss would exacerbate irreversible transition metal migration, resulting in a drastic voltage decay and capacity degeneration. Herein, a metastable layered Li-excess cathode material, T2-type $Li_{0.72}[Li_{0.12}Ni_{0.36}Mn_{0.52}]O_2$, was developed, in which both oxygen stacking arrangement and Li coordination environment fundamentally differ from that in conventional O3-type layered structures. By means of the reversible Li migration processes and structural evolutions, not only can voltage decay be effectively restrained, but also excellent capacity retention can be achieved upon long-term cycling. Moreover, irreversible/reversible anionic/cationic redox activities have been well assigned and quantified by various *in/ex-situ* spectroscopic techniques, further clarifying the charge compensation mechanism associated with (de)lithiation. These findings of the novel T2 structure with the enhanced anionic redox stability will provide a new scope for the development of high-energy-density Li-rich cathode materials.

Received: 26-Aug-2021

Revised: 28-Oct-2021

Accepted: 05-Nov-2021

Keywords: cathode materials, layered oxides, voltage decay, lattice oxygen release, structural stability

1. Introduction

Li-rich transition metal oxides with a general chemical formula of $x$$Li_2MnO_3$·(1−$x$)$LiTMO_2$ (TM = Mn, Ni, Co etc.) hold the greatest promise for the next-generation high-energy-density cathode materials because of their high output capacity promoted by oxygen redox chemistry [1,2]. In typical layered Li-rich oxides (Li/TM >1 in formula), excess lithium ions substitute for sectional transition metals, forming Li_2MnO_3 domain with LiO_6 units in TM layer, which triggers remarkable oxygen-centered capacities in high-voltage regions [3,4]. However, layered Li-rich oxides generally suffered from rapid decay of both discharge capacity and operating voltage during cycling, which can be ascribed to the irreversible oxygen loss and structural rearrangement, further hindering the development of practical applications [5,6]. More specifically, gaseous oxygen release during charging process is extremely destructive against the reversibility of anionic/cationic redox reactions and structure stability [7–10]. Within typical layered Li-rich oxides such as Li_2MnO_3 and $Li_{1.2}Ni_{0.2}Mn_{0.6}O_2$, the capacities contributed by initial oxygen oxidation (charging) cannot be effectively recovered upon anionic reduction (discharging), generating severe decay of output capacity and over reduction of transition metals [11–13]. Moreover, lattice oxygen loss severely aggravates irreversible TM migration (from

original TM layer to Li layer), resulting in a layered/spinel/disordered phase transition and consequent voltage decay during long-term cycling [14,15].

To solve these intrinsic issues, numerous research works have been carried out via intrinsic and extrinsic modification methods to improve the electrochemical/structural stability of conventional O3-type layered Li-rich oxides [2,16–19]. For instance, the substitution/doping with specific metals can stabilize oxygen redox by strengthening the hybridization of O 2p orbital with transition metal orbital [20–24]. Moreover, surface coating can effectively enhance the structure stability of electrode/electrolyte interfaces by constructing a protective layer, further suppressing gaseous oxygen release upon Li^+ deintercalation [18,25–32]. However, a less explored, yet potentially effective strategy would be to design alternative oxygen stacking arrangements and coordination environments that are less conducive to detrimental transitions; indeed, most of modifications to stabilize the anionic/cationic redox activities in Li-rich layered oxides are based on the O3-type structure [33,34]. Furthermore, the complex anionic/cationic redox behaviors shown in galvanostatic electrochemical curves hinder the elucidation of the charge compensation mechanisms due to the lack of quantitative methods on oxygen/TM-centered redox reactions [35].

Herein, a metastable Li-excess orthorhombic T2-type $Li_{0.72}[Li_{0.12}Ni_{0.36}Mn_{0.52}]O_2$ as cathode material was developed by chemical ion exchange strategy from a layered P2-type Na precursor. Unlike O3-type layered cathodes with ABCABC oxygen arrangement and octahedral site of alkali metal (AM), the T2-type cathode displays

ABB'A' oxygen stacking sequence in a two-layer unit cell, in which Li ions occupy tetrahedral sites within the AM layer. By means of the stable evolutions of its phase transitions and reversible Li migration within this structure, limited voltage decay and excellent discharge capacity retention (capacity drop of 0.24% per cycle, 100 cycles at low current density of 10 mA/g) were successfully achieved. Moreover, the capacity contributions of anionic/cationic redox activities were quantified by hard X-ray absorption spectroscopy (XAS) and acid titrated gas chromatography mass spectrometry (AT-GCMS) as well as differential electrochemical mass spectroscopy (DEMS), demonstrating the reversible oxygen-centered and TM-based redox reactions can be achieved upon cycling.

2. Experimental

2.1. Material synthesis

$Na_{0.72}[Li_{0.12}Ni_{0.36}Mn_{0.52}]O_2$ was synthesized via solid-state reactions with stoichiometric amounts of Na_2CO_3 (Wako, 2 mol% excess), Li_2CO_3 (Wako, 2 mol% excess), NiO (Wako) and MnO_2 (Wako). The powders were ball milled altogether for 24 h with the speed of 350 r/min, following by pressing into pellets and calcination at 900 °C in air for 20 h. After quenching, the Na-deficient precursor $Na_{0.72}[Li_{0.12}Ni_{0.36}Mn_{0.52}]O_2$ was stored in the glove box to further ion exchange and electrode preparation.

$Li_{0.72}[Li_{0.12}Ni_{0.36}Mn_{0.52}]O_2$ was synthesized from the Na-deficient precursor through a facile ion exchange method within molten salts. Firstly, $Na_{0.72}[Li_{0.12}Ni_{0.36}Mn_{0.52}]O_2$ was mixed with a 10-time Li excess of the eutectic

mixture of 88 mol% $LiNO_3$ (Wako) and 12 mol% LiCl (Wako), and milled together for 1 h in a dry room to avoid moist air. Then, the mixture was put into a furnace and the reaction was performed at 280 °C for 1 h in air. After ion exchange with equivalent Li, $Li_{0.72}[Li_{0.12}Ni_{0.36}Mn_{0.52}]O_2$ can be obtained after washing with distilled water and dried at 60 °C overnight.

2.2. Material characterization

The structures of $Na_{0.72}[Li_{0.12}Ni_{0.36}Mn_{0.52}]O_2$ and $Li_{0.72}[Li_{0.12}Ni_{0.36}Mn_{0.52}]O_2$ were identified by powder XRD (Ultima III, Rigaku Corporation) using radiation from Cu Kα (λ = 1.5406 Å). The contents of Na, Mn, Ni and Li in $Na_{0.72}[Li_{0.12}Ni_{0.36}Mn_{0.52}]O_2$ and $Li_{0.72}[Li_{0.12}Ni_{0.36}Mn_{0.52}]O_2$ were obtained by ICP (M90, Bruker). X-ray photoelectron spectroscopy (XPS) with Ar^+ etching was conducted in a Thermo Fisher Scientific Model Kα spectrometer equipped with Al Kα radiation (1486.6 eV). The details of the characterizations of solid state nuclear magnetic resonance (ssNMR), XAS, DEMS and AT-GCMS are shown in the Supplementary materials.

2.3. Electrochemical measurement

2032 coin-type cells were used for electrochemical measurements. All electrodes were consisted of active material, acetylene black, and polytetrafluoroethene (PTFE, 12 wt.%) binder with the weight ratio of 70:20:10. 1 mol/L $LiClO_4$/$NaClO_4$ in propylene carbonate was prepared as the electrolyte and a glass fiber film was employed as the separator. The galvanostatic charge–discharge tests were performed by using a Hokuto Denko HJ1001SD8 battery tester at different conditions. An

experimental checklist for reporting battery performances is also shown in the Supplementary materials.

3. Results and Discussion

3.1. Synthesis, structural characterization, and electrochemical performance

T2-type $Li_{0.72}[Li_{0.12}Ni_{0.36}Mn_{0.52}]O_2$ (labelled as LLNMO) was synthesized by chemical Li^+/Na^+ ion exchange from $Na_{0.72}[Li_{0.12}Ni_{0.36}Mn_{0.52}]O_2$ (Fig. 1a). The Na-based precursor is verified as a prototypical P2-type oxide by XRD Rietveld refinement (Fig. S1 and Table S1 online), in which the oxygen is stacked in an ABBA arrangement sequence and Na ions occupy prismatic sites within AM layer. The (1/3, 1/3, 0) superstructure peaks in 20°–30° is absent, indicating the absence of ordering of Li/Mn(Ni) in the TMO_2 slabs [36,37]. In addition, the contents of cationic elements in synthesized $Na_{0.72}[Li_{0.12}Ni_{0.36}Mn_{0.52}]O_2$ were confirmed by inductively coupled plasma (ICP) (Table S2 online). Moreover, the charge/discharge profiles of the Na precursor represented the relatively reversible anionic/cationic redox behaviors during initial cycles, which is consistent with reported Li-excess Na-based compounds (Fig. S2 online) [38,39]. Here, the Li-excess state is represented by the fact that Li^+ ions are located within TM layer in both Li- and Na-based layered compounds.

After the chemical Li^+/Na^+ ion exchange process, the Li-excess state and disordered Li/Ni/Mn arrangement in TM layer were well preserved [40–42]. Na^+ in the AM layers was replaced by Li^+ ions, resulting in a change in the coordination environment from the original prismatic site (P-site) to a unique tetrahedral site

(T-site) [43,44]. The (002) diffraction peak of LLNMO was located at around 17.7° (Fig. 1b), suggesting the P/T transition of coordination environment in LiO_2 slabs have been achieved because the characteristic peak of prismatic Na sites with shorter interlayer distance along *c*-axis direction could not be observed. Furthermore, the diffraction angle of (002) peak is also lower than that of the layered characteristic (003) peak in conventional O3-type structures, indicating the coordination environment of Li site is not octahedral [45]. According to XRD Rietveld refinement results (Fig. 1b and Table S3 online), these experimental peaks were indexed with an orthorhombic T2-type structure with the space group *Cmca*, displaying a Li-excess state within TM layer. The difference between the experimental and standard reference (T2-type $Li_{2/3}Ni_{1/3}Mn_{2/3}O_2$ with the space group of *Cmca*) is the absence of superstructure peaks at 20°–30°, verifying the disordered arrangement within the TM layer was also preserved in T2-type LLNMO. The T2-type structure exhibits the ABB'A' oxygen stacking arrangement, which is an intermediate state during the phase transition from P2 to O2 phase with an oxygen stacking of ABCB. Both T2 and O2 structures in Li-based compounds can be achieved from P2-type Na precursor with oxygen stacking of ABBA via ion exchange strategy. The O2 structure is achieved by gliding of the second layer from B to C, delivering the ABCB oxygen stacking and the octahedral sites for Li^+ ions. However, the T2 structure was obtained after gliding of the second layer by the distance of half the small hexagonal lattice constant, in which Li ions can be located within tetrahedral sites. Thus, the B' means the midpoint position between B and C sites, and the A' position is the midpoint between A and B

sites, respectively. The calculated lattice parameters of LLNMO are a= 8.6033(5) Å, b= 4.9514(1) Å, c= 10.0530(8) Å, V= 428.249 Å^3 and $\alpha = \beta = \gamma = 90°$ with favorable results of χ^2 (1.76) and R_{wp} (5.41%). Lastly, the chemical formula of LLNMO was obtained by ICP measurement (Table S4 online), demonstrating that the valence of Ni and Mn at pristine state is +3 and +4, respectively.

The charge/discharge profiles of LLNMO were measured by galvanostatic tests to evaluate the electrochemical behaviors during the first two Li^+ (de)intercalation processes (Fig. 1c). Starting from oxidation, the LLNMO electrode displayed two plateaus with an average voltage of 4.25 and 4.75 V, respectively, accumulating total capacities (138.5 mAh/g) equivalent to the 0.45 mol Li removal, which delivered the final composition of $Li_{0.387}Ni_{0.36}Mn_{0.52}O_2$. The corresponding charge capacity exceeded the theoretical capacity assuming only a contribution of the $Ni^{3+/4+}$ redox couple (110.2 mAh/g), indicating that oxygen-centered redox reactions were involved since Mn^{4+} in typical layered oxides cannot be further oxidized even at high potentials. Upon reduction, the slope of the potential-composition profile indicated excessive Li^+ ions inserted in layered structure to reach a composition of $Li_{0.989}Ni_{0.36}Mn_{0.52}O_2$, displaying a high output discharge capacity of ≈184 mAh/g. This high capacity was almost maintained upon the second charge, with only a limited irreversible capacity (≈7 mAh/g), implying high electrochemical reversibility within LLNMO after the first charge. Furthermore, high stability with limited voltage decay was also observed upon long-term cycling of LLNMO. At low current density of 10 mA/g, a limited capacity decay of 0.24% per cycle with nearly 100% coulombic efficiency was obtained after

100 cycles at a wide potential window of 2.0–4.8 V (Fig. 1d). Besides, slight change in average discharge voltage can be achieved during long-term cycling (Fig. 1d insert). These results indicate excellent electrochemical reversibility can be obtained in LLNMO electrode upon cycling.

3.2. Structural evolution

Operando XRD was employed to investigate the phase transition of LLNMO during initial two delithiation/lithiation processes (Fig. 2a and Fig. S3 online). During the initial charging, the characteristic peaks of T2 phase slightly shifted to lower angle and then rapidly disappeared, while a series of new well-resolved peaks arose at higher angle, corresponding to the transition of the oxide from T2 to O2 stacking and, thus, involving a change in Li coordination environment in the AM layer from tetrahedral to octahedral. The T2/O2 phase transition was generally observed in layered T2-type $LiTMO_2$ because the Li removal leads to the gliding of the TMO_2 slabs during charging, which induces that an evolution of oxygen stacking from ABB'A' (T2-type) to ABCB (O2-type) [44]. The interlayer distance along *c*-axis direction was significantly decreased during the phase transition because the smaller octahedral LiO_6 unit occupies the AM layer. Upon further delithiation, the characteristic peaks of the O2 phase gradually shifted to higher angle accompanied by Li^+ deintercalation. Furthermore, the O2 phase was preserved during the first discharge, with the peaks shifting back in a manner symmetric with charge, whereas the pristine T2 phase was not recovered. Two *ex-situ* XRD patterns corresponding LLNMO electrodes after the first charge and discharge displayed a hexagonal

O2-type structure with space group of *P6$_3$mc*, further demonstrating the irreversible phase transition from T2 to O2 phase during initial charging (Fig. S4 and Table S5, S6 online). *Operando* XRD patterns in the second cycle were also completely dominated by the evolution of the O2 phase of LLNMO electrode. Moreover, the structural evolution process during the second cycle is similar with that of the first cycle, suggesting LLNMO electrode experienced a reversible structural evolution after the initial charge, which is beneficial for achieving the stable structural and electrochemical processes upon cycling.

To study Li migration and the associated structural evolution upon (de)lithiation processes, ^{7}Li solid state nuclear magnetic resonance (ssNMR) spectroscopy was conducted during the initial two cycles (Fig. 2b). It is an effective measurement to achieve explicit identification of Li local environment and reliable quantification at different charged states. Generally, the resonances at 1300–1650 ppm correspond to hyperfine interactions of Li sites in TM layers (Li_{TM}), whereas the resonances of Li^+ ions in the AM layer (Li_{AM}) were located at the lower region of 500–1000 ppm [46]. The sharp peaks located at around 0 ppm can be ascribed to diamagnetic impurity phases such as Li_2CO_3 and/or LiF, which stems from the formation of cathode-electrolyte interphase layers [47]. Moreover, the broad signals of main resonances and spinning sidebands were caused by many Li positions (tetrahedral and octahedral sites) and complex adjacent environments within layered oxides with disordered arrangements or/and defects generated during ion exchange process. Herein, because of the overlaps between spinning sidebands with the actual resonance

and the complex Li neighboring environments, the actual Li resonances are simplified as two sites of Li_{AM} and Li_{TM}, in which the quantification has a certain degree of uncertainty. For pristine T2 LLNMO, integration of the two broad resonances centered at 713 (shaded grey) and 1520 ppm (shaded blue) showed that 85.7% Li^+ ions were found in the AM layer and 14.3% Li^+ ions within the TM layer, respectively, which is consistent with design formula of $Li_{0.72}[Li_{0.12}Ni_{0.36}Mn_{0.52}]O_2$. After charging, the intensity of the two broad Li resonances gradually decreased, which is consistent with the Li^+ ions extraction from the layered structure. The Li^+ deintercalation from AM layer might induce the gliding of the TMO_2 slabs and the change of coordination environment, which is a possible reason for the phase transition from T2 to O2 structure. According to the electrochemical results, about 0.453 mol Li^+ ions removed from layered structure, whereas 0.387 mol Li^+ ions can be well preserved after initial charge. Combining with the absence of the signal of Li^+ ions within TM layer, it can be deduced that almost all of Li^+ ions reside in AM layer, resulting in the existence of vacancy of Li within TM layer. After discharge to 2 V, 0.925 mol Li_{AM} (93.5%) and 0.064 mol Li_{TM} (6.5%) were recovered, indicating that Li (de)intercalation is a relatively reversible process within AM and TM layer. On the contrary, O3/O'3-type Li-rich layered oxides generally suffer from irreversible Li^+ (de)intercalation processes [48]. In particularly, Li_2MnO_3 cathode shows significant lithium removal (up to 85%) from the lattice on the first-cycle charge, whereas up to 30% of the Li can be reinserted in the host lattice upon initial discharge, resulting in a large number of vacancies both in AM and TM layers [49,50]. As a result, the Li–O–

Li configurations cannot be recovered during subsequent charge since most Li^+ ions cannot be reinserted within TM layers, which severely limits the application of capacity triggered by oxygen redox reactions. Furthermore, these defects seriously exacerbate irreversible TM migration from TM layer to AM layer, giving rise to destructive phase transition of layered to spinel even to disordered structures, which is directly related to structural and electrochemical fade mechanisms. In contrast, for LLNMO electrode, the Li signal in TM layer was absent, and the content of Li within AM layer increased to about 0.395 mol after the second charge, delivering a similar chemical state compared to the first charged state. It indicates the stable Li migration evolutions can be realized in TM and AM layers after the initial charge, which effectively enhances the structural stability within LLNMO electrode upon cycling.

3.3. Valence state analysis of Mn and Ni

Mn and Ni K-edge hard XAS were employed to investigate the redox changes at cationic centers and elucidate the charge compensation mechanisms within LLNMO electrode during Li^+ (de)intercalation processes (Fig. 3a and 3b). The evolutions of the Mn and Ni oxidation states was obtained from the changes in the threshold of the absorption edge at different charged states [51]. The absorption threshold is determined by the transition to the lowest unoccupied states. The states at the Fermi level in metals involve the rising edge in XAS spectra. The rising edge arises from the electric dipole-allowed transition from 1s to 4p orbital, which is beneficial for deducing the oxidation states of Mn and Ni (Fig. 3c and 3d). Furthermore, by comparison with the shift of rising edge and the position of first inflection point, the

first derivative of these spectra also can be used to clearly derive the trends in rising edge (Fig. 3e and 3f). Upon oxidation of LLNMO to 4.8 V, the absorption edge of Ni K-edge moved to higher photon energy, while there was almost no energy shift of the Mn rising edge, suggesting an obvious increase in Ni oxidation state and a slight change of Mn valence upon the first charge. Furthermore, the spectrum of Ni K-edge shifted to the original location after discharged to 3 V and then experienced no virtual change from 3.0 to 2.0 V, displaying a highly reversible redox process of Ni occurring primarily at high potential, with the metal not significantly involved in the capacities generated at lower potential. In contrast, an obvious shift of the Mn K-edge can only be detected after discharged to 2.0 V, suggesting Mn-based reduction reactions primarily occurred at low potential during discharging. Moreover, when recharge to 4.8 V, the absorption edge of Mn and Ni both shifted to higher photon energy, reaching a similar position with that at first charged state, indicating they were both redox active. Thus, it is rational to deduce that Mn and Ni redox reactions in LLNMO undergo a relatively reversible process after the first charge.

To gain further insight into these cationic reactions upon cycling, the oxidation state was roughly estimated by applying the integral method first proposed by Dau et al. [51]. To subsequently assess the existence anionic redox reactions, we compared the values of capacity associated with these redox changes with the total charge/discharge capacity (from electrochemical results, Fig. 1c). Using appropriate references for the Mn/Ni K-edge, the integral method gives a linear relationship between oxidation states (+2, +3 and +4) and corresponding edge positions (Figs. S5

and S6 online). This curve was used as calibration to extract approximate average Mn/Ni oxidation state of LLNMO from measured edge position by using the same method (Fig. S7 online). The detailed data processing of standard references of Ni/Mn XAS spectra by integral method is also shown in Figs. S5 and S6 (online). Besides, limited by the accuracy of this technique, the integral method is simply employed as a quasi-quantitative measure to obtain the average TM oxidation states. Herein, the valence of Mn and Ni in LLNMO is approximate +4.0 and +3.0 at the pristine state, respectively, in good agreement with our design and ICP results. Upon initial charging, the average Ni oxidation state is considerably increased to +3.5, delivering the charge capacity of ≈55 mAh/g. In contrast to Ni, it is abnormal that the oxidation state of Mn has a slight decrease after initial charging, indicating superoxo species and/or O_2 release enlists a partial reduction of neighboring Mn^{4+} to Mn^{3+} based on the reductive coupling mechanism [21]. Moreover, it is probably caused by quantitative errors of the integral method, suggesting the Mn has no obvious change upon first charging. Clearly, the capacity accumulated upon this first charge was too high to be explained by redox changes at the Ni centers. Therefore, oxygen-centered oxidation reactions (O^{2-} to O^{n-}/O_2, n<2) are proposed to contribute up to ≈83 mAh/g during initial charging. Upon initial discharging, the oxidation state of Mn and Ni decreased to about +3.5 and +3.0, corresponding to 53 and 59 mAh/g, respectively. Again, these values add to less than the observed capacity, suggesting that part of the discharge capacity is contributed by oxygen-centered reduction. An estimation based on the total capacity indicates up to 72 mAh/g from oxygen redox, suggesting an irreversible

capacity of ≈11 mAh/g with respect to the activity ascribed to oxygen in the first charge. The difference might originate from side reactions such as oxygen release and/or electrolyte decomposition. After recharging to 4.8 V, Mn and Ni was oxidized to the values, which is similar to the first charged state, demonstrating that the Mn/Ni redox reactions are reversible after the initial Li^+ deintercalation process. Estimations of the oxygen-centered oxidation by comparing total capacity to the observed oxidation of Mn and Ni brought about a value of ≈74 mAh/g, which is roughly equivalent to the initial discharge capacity, implying oxygen redox reactions are also relatively reversible after first charging. As a result, the estimated capacity distributions of Ni/Mn-based and oxygen-centered redox activities during the initial two cycles can be extracted (Fig. S8 online), which is significant for the understanding of charge compensation mechanisms in Li-rich cathode materials.

3.4. Analysis of oxygen behaviors

The oxygen-centered redox behaviors in LLNMO were further assigned and quantified by *ex-situ* XPS and *operando* DEMS as well as AT-GCMS (Fig. 4a–4e). For the pristine LLNMO, the signal with lower binding energy of lattice oxygen (O^{2-}) was located at 529.5 eV. Moreover, the peaks with high energy can be typically identified as carbonate species (531.6 eV) and oxygenated species (533.1 eV) on the surface, respectively (Fig. 4a) [52]. Upon charging, an obvious shoulder appeared at 530.7 eV, which is commonly generated by the formation of oxidized lattice oxygen (O^{n-}), indicating anionic redox reactions are triggered upon initial charging. Furthermore, the O^{n-} signal disappeared after discharged to 3.0 V and cannot be

detected at the end of discharge process, suggesting O^{n-} has been reduced to lattice oxygen in high voltage region. Notably, the O^{n-} peak can be probed again when the sample is recharged to 4.8 V, indicating a relatively reversible oxygen redox reaction within the initial two Li^+ (de)intercalation processes. Furthermore, Ar^+ etching was employed to investigate the changes in these signatures at a probing depth from several nanometers to ≈100 nm. With increased etching time, O^{n-} peak can be continuously observed in the charged state and can be well reduced to lattice oxygen during discharging (Fig. 4b and 4c), demonstrating the oxygen redox reactions are reversible at both on surface and interior of the materials. Besides, Lebens-Higgins et al. [53] also proposed the O^{n-} signal might conceivably be generated by the irreversible TM reduction and electrolyte decomposition on surface.

In terms of the irreversible oxygen behavior, based on DEMS, only 126 μmol/g O_2 could be detected at the end of the initial charge owning to excessive oxidation reactions centered at oxygen, delivering ≈13.55 mAh/g based on a $4e^-$ process from lattice oxide to O_2 (Fig. 4d). Furthermore, it is worth mentioning that there is no increase of gaseous oxygen release during the subsequent constant current–constant voltage (CC–CV) process. Moreover, serious oxygen release cannot be observed by operando DEMS in subsequent processes, including the second CC–CV time, indicating more moderate oxygen behaviors can be triggered after initial charging. Besides, a small amount of CO_2 was also detected in the first two charges, which could arise from electrolyte degradation at high voltages or/and reaction with generated electron-depleted oxo species. The exact origin cannot be accurately

established based on the data available. AT-GCMS offered a complementary quantitative measure to assess the contributions of oxygen redox reactions, as reported in a previous study of Li-rich cathode materials showing oxygen redox [54]. By quantifying the amount of O_2 evolved from electrodes after acid titrations, the capacity of oxygen oxidation reactions can be calculated based on the oxygen evolution reaction between H^+/H_2O and oxidized lattice oxygen [55]. These titrations demonstrate contributions from oxygen redox during first and second charging (71.35 and 73.94 mAh/g) and the oxidized oxygen has been completely reduced during discharging, which agrees with the O-related capacity contributions quantified by XAS (Fig. 4e). Altogether, benefiting from the combination of XAS and operando DEMS as well as AT-GCMS, the charge compensation mechanism within LLNMO electrode has been clarified by estimating the oxidation states of Ni/Mn and the capacity contribution of oxygen redox during the initial two cycles (Fig. 4f). After an initial structural rearrangement (T2/O2 phase transition) and slight lattice oxygen loss (1.1%), LLNMO harvests relatively reversible electrochemical processes centered at the TMs and lattice oxygen during subsequent cycles. Besides, the capacity distributions of anionic redox reactions (40%, ≈72 mAh/g) and cationic redox reactions (60%, ≈112 mAh/g) can be distinctly allocated during the initial discharge.

3. Conclusion

In this work, we developed a Li-excess T2-type $Li_{0.72}[Li_{0.12}Ni_{0.36}Mn_{0.52}]O_2$ as the cathode material with the ABB′A′ oxygen stacking arrangement and tetrahedral AM site, which fundamentally resolves the inherent problems of oxygen release and

structural distortion in conventional Li-rich oxides. Benefitting from the rational structure design of oxygen stacking arrangement, a relatively reversible Li migration process can be harvested both in AM and TM layers, distinctly demonstrated through ssNMR measurement. Not only the durative output capacities triggered by anionic redox activities can be obtained due to the stable Li–O–Li (Vac.) configuration, but also the layered/spinel phase transition caused by irreversible TM migration can be effectively suppressed because of the modified oxygen stacking sequence, which provides a solid foundation of excellent capacity retention and limited voltage decay upon long term cycling. Moreover, combined with *in/ex-situ* characterizations (DEMS, hard XAS and AT-GCMS etc.), the irreversible/reversible TMs/O-related redox reactions have been distinctly assigned, clarifying the charge compensation mechanism of anionic/cationic redox reactions. Altogether, these findings of the novel T2 structural framework and optimized oxygen redox chemistry will offer further unexplored opportunities in securing next-generation Li-rich cathodes with unique structures and high energy density.

Conflict of interest

The authors declare that they have no conflict of interest.

Acknowledgments

Xin Cao acknowledges the scholarship from the China Scholarship Council (CSC). Haifeng Li and Jordi Cabana were supported by the National Science Foundation under Grant No. DMR-1809372. This research used resources of the Advanced Photon Source, a U.S. Department of Energy (DOE) Office of Science User Facility operated for the DOE Office of Science by Argonne National Laboratory under Contract No. DE-AC02-06CH11357. We thank Advanced Photon Source at Argonne National Laboratory.

Author Contributions

Xin Cao contributed to the design of the research. Xin Cao performed the experimental data analysis. Xin Cao conducted the material design and synthesis as well as Operando XRD measurements. Yu Qiao performed the ssNMR, DEMS, AT-GCMS and XPS measurements. Jianan Zhang conducted the analyses of ssNMR. Hirokazu Kitaura polished the language and commented on the manuscript. Haifeng Li and Jordi Cabana conducted the XAS characterizations and analysis. Yu Qiao and Haoshen Zhou supervised the work. All authors co-wrote the manuscript, discussed the results, and commented on the manuscript.

References

[1] Assat G, Tarascon J-M, Fundamental understanding and practical challenges of anionic redox activity in Li-ion batteries. Nat Energy 2018; 3: 373–86.

[2] Yu Y, Karayaylali P, Sokaras D, et al. Towards controlling the reversibility of anionic redox in transition metal oxides for high-energy Li-ion positive electrodes. Energy Environ Sci 2021; 14: 2322–34.

[3] Yu Y, Karayaylali P, Nowak S H, et al. Revealing electronic signatures of lattice oxygen redox in lithium ruthenates and implications for high-energy Li-ion battery material designs. Chem Mater 2019; 31: 7864–76.

[4] Xiao B, Liu H, Chen N, et al. Size-mediated recurring spinel sub-nanodomains in Li- and Mn-rich layered cathode materials. Angew Chem Int Ed 2020; 59: 14313–20.

[5] Gu L, Xiao D, Hu Y S, et al. Atomic-scale structure evolution in a quasi-equilibrated electrochemical process of electrode materials for rechargeable batteries. Adv Mater 2015; 27: 2134–49.

[6] Mohanty D, Sefat A S, Li J, et al. Correlating cation ordering and voltage fade in a lithium-manganese-rich lithium-ion battery cathode oxide: a joint magnetic susceptibility and TEM study. Phys Chem Chem Phys 2013; 15: 19496–509.

[7] House R A, Rees G J, Pérez-Osorio M A, et al. First-cycle voltage hysteresis in Li-rich 3d cathodes associated with molecular O_2 trapped in the bulk. Nat Energy 2020; 5: 777–85.

[8] Lee J, Papp J K, Clément R J, et al. Mitigating oxygen loss to improve the cycling

performance of high capacity cation-disordered cathode materials. Nat Commun 2017; 8: 981.

[9] Hwang J, Myeong S, Jin W, et al. Excess-Li localization triggers chemical irreversibility in Li- and Mn-rich layered oxides. Adv Mater 2020; 32: 2001944.

[10] Yahia M B, Vergnet J, Saubanère M, et al. Unified picture of anionic redox in Li/Na-ion batteries. Nat Mater 2019; 18: 496–502.

[11] Nakayama K, Ishikawa R, Kobayashi S, et al. Dislocation and oxygen-release driven delithiation in Li_2MnO_3. Nat Commun 2020; 11: 4452.

[12] Rana J, Stan M, Kloepsch R, et al. Structural changes in Li_2MnO_3 cathode material for Li-ion batteries. Adv Energy Mater 2014; 4: 1300998.

[13] Wu F, Kim G-T, Diemant T, et al. Reducing capacity and voltage decay of Co-free $Li_{1.2}Ni_{0.2}Mn_{0.6}O_2$ as positive electrode material for lithium batteries employing an ionic liquid-based electrolyte. Adv Energy Mater 2020; 10: 2001830.

[14] Boulineau A, Simonin L, Colin J F, et al. First evidence of manganese–nickel segregation and densification upon cycling in Li-rich layered oxides for lithium batteries. Nano Lett 2013; 13: 3857–63.

[15] Gu M, Belharouak I, Zheng J, et al. Formation of the spinel phase in the layered composite cathode used in Li-ion batteries. ACS Nano 2013; 7: 760–7.

[16] Zhao S, Yan K, Zhang J, et al. Reaction mechanisms of layered lithium-rich cathode materials for high-energy lithium-ion batteries. Angew Chem Int Ed 2021; 60: 2208 –20.

[17] Wu F, Kim G T, Diemant T, et al. Reducing capacity and voltage decay of

Co-free $Li_{1.2}Ni_{0.2}Mn_{0.6}O_2$ as positive electrode material for lithium batteries employing an ionic liquid-based electrolyte. Adv Energy Mater 2020; 10: 2001830.

[18] Lei Y, Ni J, Hu Z, et al. Surface modification of Li-rich Mn-based layered oxide cathodes: challenges, materials, methods, and characterization. Adv Energy Mater 2020; 10: 2002506

[19] Liu P, Zhang H, He W, et al. Lithium deficiencies engineering in Li-rich layered oxide $Li_{1.098}Mn_{0.533}Ni_{0.113}Co_{0.138}O_2$ for high-stability cathode. J Am Chem Soc 2019; 141: 10876–82.

[20] Saubanere M, McCalla E, Tarascon J M, et al. The intriguing question of anionic redox in high-energy density cathodes for Li-ion batteries. Energy Environ Sci 2016; 9: 984–91.

[21] Sathiya M, Rousse G, Ramesha K, et al. Reversible anionic redox chemistry in high-capacity layered-oxide electrodes. Nat Mater 2013; 12: 827–35.

[22] Perez A J, Jacquet Q, Batuk D, et al. Approaching the limits of cationic and anionic electrochemical activity with the Li-rich layered rocksalt Li_3IrO_4. Nat Energy, 2017; 2: 954–62.

[23] Li H, Ramakrishnan S, Freeland J W, et al. Definition of redox centers in reactions of lithium intercalation in Li_3RuO_4 polymorphs. J Am Chem Soc 2020; 142: 8160–73.

[24] Cao X, Li H, Qiao Y, et al. Stabilizing reversible oxygen redox chemistry in layered oxides for sodium-ion batteries. Adv Energy Mater 2020; 10: 1903785.

[25] Sun G, Yu F D, Zhao C, et al. Decoupling the voltage hysteresis of Li-rich

cathodes: electrochemical monitoring, modulation anionic redox chemistry and theoretical verifying. Adv Funct Mater 2020; 31: 2002643.

[26] Cui C, Fan X, Zhou X, et al. Structure and interface design enable stable Li-rich cathode. J Am Chem Soc 2020; 142: 8918–27.

[27] Chen Q, Pei Y, Chen H, et al. Highly reversible oxygen redox in layered compounds enabled by surface polyanions. Nat Commun 2020; 11: 3411.

[28] Zhang X D, Shi J L, Liang J Y, et al. Suppressing surface lattice oxygen release of Li-rich cathode materials via heterostructured spinel $Li_4Mn_5O_{12}$ Coating. Adv Mater 2018; 30: 1801751.

[29] Zheng J, Gu M, Xiao J, et al. Functioning mechanism of AlF_3 coating on the Li- and Mn-rich cathode materials. Chem Mater 2014; 26: 6320–7.

[30] Kurilenko K A, Shlyakhtin O A, Petukhov D I, et al. Catalytic effect of nanostructured CeO_2 coating on the electrochemical performance of $Li(Li,Ni,Mn,Co)O_2$. Solid State Ion 2018; 324: 59–64.

[31] Qing R-P, Shi J-L, Xiao D-D, et al. Enhancing the kinetics of Li-rich cathode materials through the pinning effects of gradient surface Na^+ doping. Adv Energy Mater 2016; 6: 1501914.

[32] Kim S, Cho W, Zhang X, et al. A stable lithium-rich surface structure for lithium-rich layered cathode materials. Nat Commun 2016; 7: 13598.

[33] Eum D, Kim B, Kim S J, et al. Voltage decay and redox asymmetry mitigation by reversible cation migration in lithium-rich layered oxide electrodes. Nat Mater 2020; 19: 419–27.

[34] Cao X, Li H, Qiao Y, et al. Stabilizing anionic redox chemistry in a Mn-based layered oxide cathode constructed by Li-deficient pristine state. Adv Mater 2021; 33: 2004280.

[35] Chen H, Islam M S. Lithium extraction mechanism in Li-rich Li_2MnO_3 involving oxygen hole formation and dimerization. Chem Mater 2016; 28: 6656–63.

[36] Zou Y, Li B, Ning J, et al. A high-capacity O2-type Li-rich cathode material with a single-layer Li_2MnO_3 superstructure. Adv Mater 2018; 30: 1707255.

[37] Ning F, Li B, Song J, et al. Inhibition of oxygen dimerization by local symmetry tuning in Li-rich layered oxides for improved stability. Nat Commun 2020; 11: 4973.

[38] Cao X, Li X, Qiao Y, et al. Restraining oxygen loss and suppressing structural distortion in a newly Ti-substituted layered oxide P2-$Na_{0.66}Li_{0.22}Ti_{0.15}Mn_{0.63}O_2$. ACS Energy Lett 2019; 4: 2409–17

[39] Cao X, Zhou H. An indicator of designing layered sodium-ion oxide materials. Sci Bull 2021; 66: 753–4.

[40] Paulsen J M, Larcher D, Dahn J R. O2 structure $Li_{2/3}[Ni_{1/3}Mn_{2/3}]O_2$: a new layered cathode material for rechargeable lithium batteries III. ion exchange. J Electrochem Soc 2000; 147: 2862–7.

[41] Cao X, Qiao Y, Jia M, et al. Ion-exchange: a promising strategy to design Li-rich and Li-excess layered cathode materials for Li-ion batteries. Adv Energy Mater 2021; DOI: 10.1002/aenm.202003972.

[42] Cao X, Li H, Qiao Y, et al. Achieving stable anionic redox chemistry in Li-excess

O2-type layered oxide cathode via chemical ion-exchange strategy. Energy Storage Mater 2021; 38: 1–8.

[43] Paulsen J M, Donaberger R A, Dahn J R. Layered T2-, O6-, O2-, and P2-type $A_{2/3}[M'^{2+}_{1/3}M^{4+}_{2/3}]O_2$ bronzes, A = Li, Na; M' = Ni, Mg; M = Mn, Ti. Chem Mater 2000; 12: 2257–67.

[44] Lu Z, Dahn J R. Intercalation of water in P2, T2 and O2 structure $Az[CoxNi_{1/3-x}Mn_{2/3}]O_2$. Chem Mater 2001; 13: 1252–7.

[45] Shao-Horn Y, Weill F, Croguennec L, et al. Lithium and vacancy ordering in $T^{\#}2–Li_xCoO_2$ derived from O2-type $LiCoO_2$. Chem Mater 2003; 15: 2977–83.

[46] Li X, Tang M, Feng X, et al. Lithiation and delithiation dynamics of different Li sites in Li-rich battery cathodes studied by operando nuclear magnetic resonance. Chem Mater 2017; 29: 8282–91.

[47] Dogan F, Croy J R, Balasubramanian M, et al. Solid state NMR studies of Li_2MnO_3 and Li-rich cathode materials: proton insertion, local structure, and voltage fade. J Electrochem Soc 2014; 162, A235–43.

[48] Salager E, Sarou-Kanian V, Sathiya M, et al. Solid-state NMR of the family of positive electrode materials $Li_2Ru_{1-y}Sn_yO_3$ for lithium-ion batteries. Chem Mater 2014; 26: 7009–19.

[49] Oishi M, Fujimoto T, Takanashi Y, et al. Charge compensation mechanisms in $Li_{1.16}Ni_{0.15}Co_{0.19}Mn_{0.50}O_2$ positive electrode material for Li-ion batteries analyzed by a combination of hard and soft X-ray absorption near edge structure. J Power Sources, 2013; 222: 45–51.

[50] Yang Y, Su H, Wu T, Atomic pair distribution function research on Li_2MnO_3 electrode structure evolution. Sci Bull 2019; 64: 553–61.

[51] Dau H, Liebisch P, Haumann M. X-ray absorption spectroscopy to analyze nuclear geometry and electronic structure of biological metal centers—potential and questions examined with special focus on the tetra-nuclear manganese complex of oxygenic photosynthesis. Anal Bioanal Chem 2003; 376: 562–83.

[52] Assat G, Iadecola A, Foix D, et al. Direct quantification of anionic redox over long cycling of Li-rich NMC via hard X-ray photoemission spectroscopy. ACS Energy Lett 2018; 3: 2721–8.

[53] Lebens-Higgins Z W, Chung H, Zuba M J, et al. How bulk sensitive is hard X-ray photoelectron spectroscopy: accounting for the cathode–electrolyte interface when addressing oxygen redox. J Phys Chem Lett 2020; 11: 2106–12.

[54] Renfrew S E, McCloskey B D, Quantification of surface oxygen depletion and solid carbonate evolution on the first cycle of $LiNi_{0.6}Mn_{0.2}Co_{0.2}O_2$ Electrodes. ACS Appl Energy Mater 2019; 2: 3762–72.

[55] Rana J, Papp J K, Lebens-Higgins Z, et al. Quantifying the capacity contributions during activation of Li_2MnO_3. ACS Energy Lett 2020; 5: 634–41.

Xin Cao currently works as a postdoctoral fellow at the National Institute of Advanced Industrial Science and Technology (AIST, Japan). He earned his B.S. degree in 2015 from Shaanxi University of Science & Technology (SUST) and M.S. degree in 2018 from Shaanxi Normal University (SNNU). He received his Ph.D. degree from Tsukuba University (Japan) in 2021. His research interest focuses on the development of high-energy-density cathode materials and electrochemical operando characterizations for Li/Na ion batteries.

Haifeng Li is now a postdoctoral scholar at Northwestern University (USA). He received his B.S. degree from Qingdao University of Science & Technology (China) and Ph.D. degree from University of Illinois at Chicago (USA). His research interest includes synchrotron-based advanced characterization, Li-rich cathode materials for rechargeable Li-ion batteries, and electrocatalysts for oxygen evolution reaction and lattice oxygen redox.

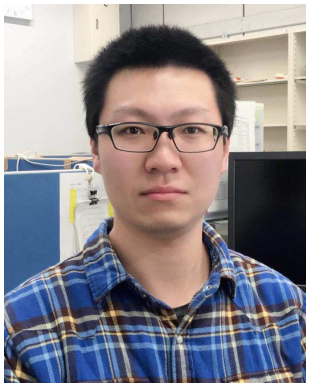

Yu Qiao is currently a professor at the College of Chemistry and Chemical Engineering, Xiamen University. He earned his B.S. degree from the University of Science and Technology of China (USTC) in 2013. He received his Ph.D. degree from Tsukuba University (Japan) in 2019, and then worked as a postdoctoral fellow at the National Institute of Advanced Industrial Science and Technology (AIST, Japan). His research interest focuses on the development of electrochemical energy storage devices, surface/interfacial electrochemistry and operando spectroscopic characterizations.

Haoshen Zhou obtained his B.S. degree from Nanjing University in 1985, and received his Ph.D. degree from the University of Tokyo in 1994. He is a professor at the College of Engineering and Applied Sciences, Nanjing University. His research interest includes the synthesis of energy active materials and their applications in Li-ion batteries, Na-ion batteries, Li redox flow batteries, metal–air batteries, and new type batteries/cells.

Fig. 1 (Color online) Synthesis, structural characterization, and electrochemical performance of T2-type LLNMO. (a) Schematic illustration of Li/Na ion exchange reaction from P2-type Na-based precursor to T2-type Li-based LLNMO. (b) The XRD patterns of pristine T2-type LLNMO. The observed pattern, the calculated pattern, the difference between the two patterns and the corresponding Bragg positions are shown. The inset is a schematic illustration of the crystal structure of the LLNMO with ABB′A′ oxygen stacking along the [110] zone axis. (c) Typical charge–discharge profiles of LLNMO within the voltage window of 2.0 to 4.8 V at a current density of 10 mA/g in Li-half cells. The mole numbers of electron were converted to mole numbers of (de)intercalated Li^+ during the initial two cycles. (d) Cycling performance of LLNMO between 2 and 4.8 V at the current density of 10 mA/g. The inset displays the normalized discharge profiles of LLNMO in the 1st, 10th, 20th and 50th cycles.

Fig. 2 (Color online) Phase evolution and Li migration processes of T2-type LLNMO during cycling. (a) *In-situ* XRD patterns of LLNMO electrode during the initial two cycles. (b) ^{7}Li solid state NMR spectra of T2-type LLNMO electrode samples of pristine state, initial charge to 4.8 V and initial discharge to 2 V.

Fig. 3 (Color online) Analysis of cationic states in T2-type LLNMO during the initial two cycles. (a) Mn and (b) Ni K-edge hard X-ray absorption spectra (XAS) of different samples (pristine, 1st charged 4.8 V, 1st discharged 3.0 V, 1st discharged 2.0 V and 2nd charged 4.8 V). The magnified rising edge region of (c) Mn and (d) Ni K-edge XAS labeled by the light orange rectangle. The corresponding 1st derivative plots of (e) Mn and (f) Ni K-edge XAS.

Fig. 4. (Color online) Analysis of O activity in T2-type LLNMO during the initial two cycles. (a) O 1s XPS spectra of T2-type LLNMO electrode at different states (pristine, 1st charged 4.8 V, 1st discharged 3.0 V, 1st discharged 2.0 V and 2nd charged 4.8 V). XPS patterns of (b) charged and (c) discharged T2-type LLNMO electrode with different etching time. (d) *Operando* differential electrochemical mass spectrometry (DEMS) of the rate of evolution of O_2 and CO_2 during cycling. (e) Results of acid titrations-gas chromatography mass spectrometry (AT-GCMS) of two electrodes harvested at the end of each of the first two charge processes. (f) Capacity contributions of oxygen redox (reversible oxygen behavior, O_2 evolution) and Ni/Mn-based redox reactions during the initial two cycles.

(a)

P2

Li/Na ion-exchange

(AM layer)

T2

A
B
AM layer
B
TM layer
A
Na
A
B

Li

Na

AM layer
TM layer
Li

Prismatic site
(P-site)

Tetrahedral site
(T-site)

(b)

XRD intensity (a.u.)

(002)

T2-type $Li_{0.72}[Li_{0.12}Ni_{0.36}Mn_{0.52}]O_2$

A
B
Li layer
B′
TM layer
A′
A
B

Li layer: Li-deficient state

TM layer: Li / Ni / Mn
(Li-excess state)

R_{wp}=5.412%

χ^2 = 1.76

Experiment
Calculated
Difference
C m c a

10 20 30 40 50 60 70 80

2θ (°)

(c)

Li in $Li_{0.72}[Li_{0.12}Ni_{0.36}Mn_{0.53}]O_2$

1st cycle

2nd cycle

10 mA/g

Potential (V vs. Li/Li+)

5.0 4.5 4.0 3.5 3.0 2.5 2.0

1.0 0.9 0.8 0.7 0.6 0.5 0.4

-50 0 50 100 150

Specific capacity (mAh/g)

(d)

Discharge cap. (mAh/g)

200 150 100 50 0

Colu. eff. (CE%)

100 95 90

Slight change in
average discharge voltage

3.32 V

3.29 V

10 mA/g

1st

10th

20th

50th

Potential (V vs. Li/Li+)

5.0 4.5 4.0 3.5 3.0 2.5 2.0

Normalized discharge capacity

0.0 0.2 0.4 0.6 0.8 1.0

0 20 40 60 80 100

Cycle number

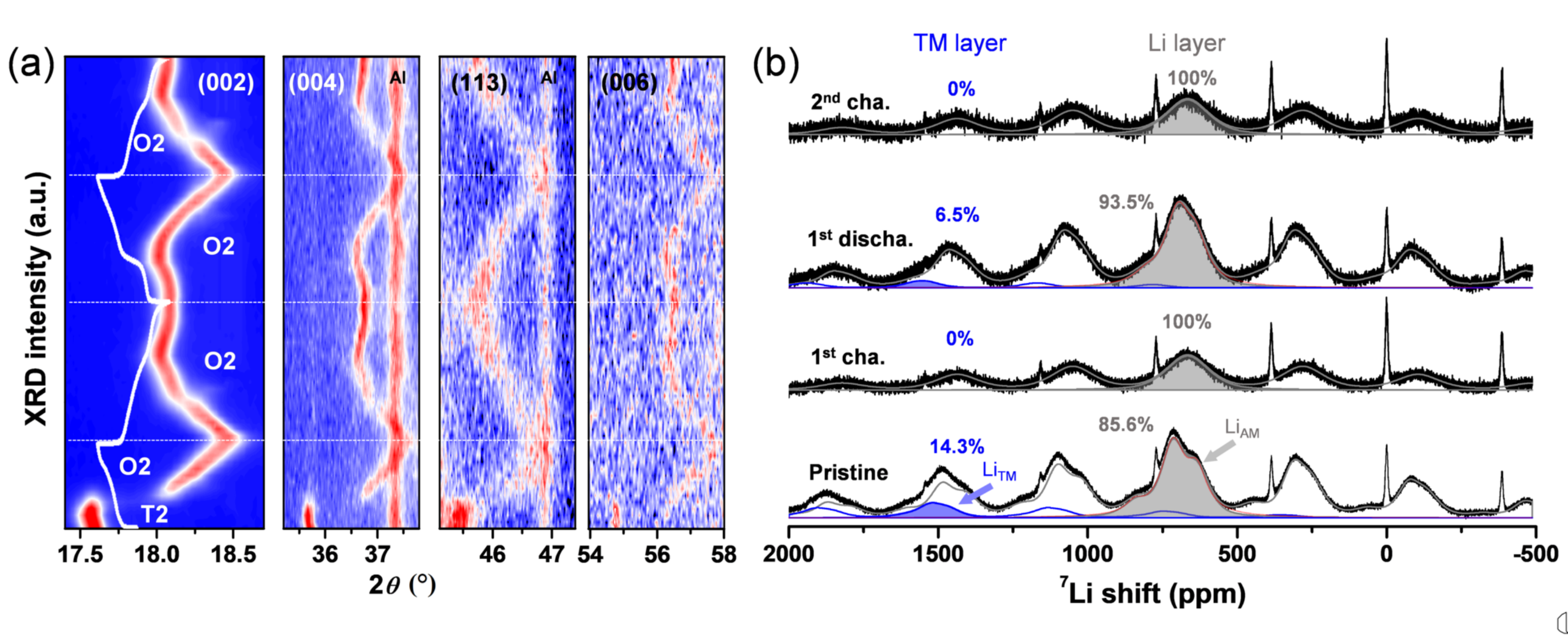
(a)
(002)
(004)
Al
(113)
Al
(006)
O2
O2
O2
O2
T2
XRD intensity (a.u.)
17.5
18.0
18.5
36
37
46
47
54
56
58
2θ (°)
(b)
TM layer
Li layer
2nd cha.
0%
100%
1st discha.
6.5%
93.5%
1st cha.
0%
100%
Pristine
14.3%
85.6%
LiTM
LiAM
2000
1500
1000
500
0
-500
7Li shift (ppm)

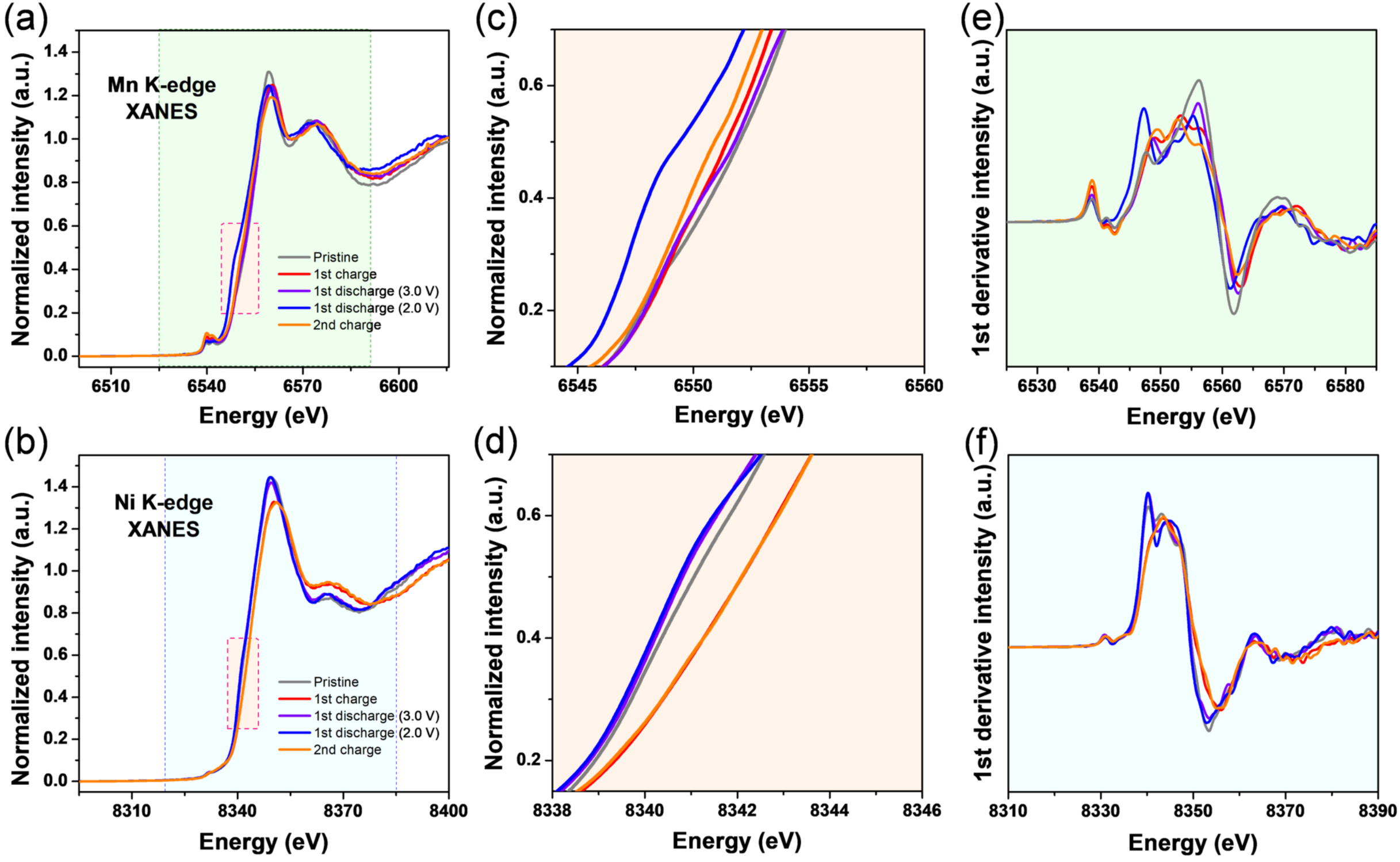
(a)
Mn K-edge
XANES
Normalized intensity (a.u.)
Energy (eV)
Pristine
1st charge
1st discharge (3.0 V)
1st discharge (2.0 V)
2nd charge
(c)
Normalized intensity (a.u.)
Energy (eV)
(e)
1st derivative intensity (a.u.)
Energy (eV)
(b)
Ni K-edge
XANES
Normalized intensity (a.u.)
Energy (eV)
Pristine
1st charge
1st discharge (3.0 V)
1st discharge (2.0 V)
2nd charge
(d)
Normalized intensity (a.u.)
Energy (eV)
(f)
1st derivative intensity (a.u.)
Energy (eV)

(a)

Lattice oxygen (O^{2-})

Oxidized lattice oxygen (O^{n-})

2nd cha. (4.8 V)

1st discha. (2.0 V)

1st discha. (3.0 V)

Oxygenated deposited species

1st cha. (4.8 V)

Fitted curve

Original curve

Carbonate species

Pristine

540 538 536 534 532 530 528 526

Binding energy (eV)

(b)

1st cha. (4.8 V)

Oxidized lattice oxygen (O^{n-})

536 534 532 530 528 526

Binding energy (eV)

2 4 6 8 10 12 14

Etching time (min)

(c)

1st discha. (2.0 V)

536 534 532 530 528 526

Binding energy (eV)

2 4 6 8 10 12 14

Etching time (min)

(d)

Gas evol. rate (μmol/(g min))

6 4 2 0

O_2

1 0

CO_2

1st cha.

CC-CV

1st discha.

2nd cha.

CC-CV

20 mA/g

loss O_2: 126.6 μmol/g

(~13.55 mAh/g; $4e^-/O_2$)

0 5 10 15 20 25

DEMS time (h)

(e)

ARR cap. (mAh/g)

76 72 68 64 60 0

~73.94 mAh/g (2nd cha.)

~72.14 mAh/g (1st discha.)

AT-GCMS

1st cha. (71.35 mAh/g)

2nd cha. (72.68 mAh/g)

O-related capacity quantified by XAS

n/a O_2

1st and 2nd discha.

0 600 640 680 720

Amount of O_2 (μmol/g~LLNMO)

(f)

Potential (V vs. Li/Li^+)

5 4 3 2

+2 +4 Mn

+2 +4 Ni

O^{2-} $(O_2)^{n-}$

(T2/O2 phase-trans)

(O2-type)

Initial charge

Lattice oxy. loss: 1.1%

Phase-trans-free

Anionic redox reactions: ~72 mAh/g 40%

Cationic redox reactions: ~112 mAh/g 60%

0 40 80 120

0 60 120 180

Specific capacity (mAh/g~LLNMO)

T2-type $Li_{0.72}[Li_{0.12}Ni_{0.36}Mn_{0.52}]O_2$

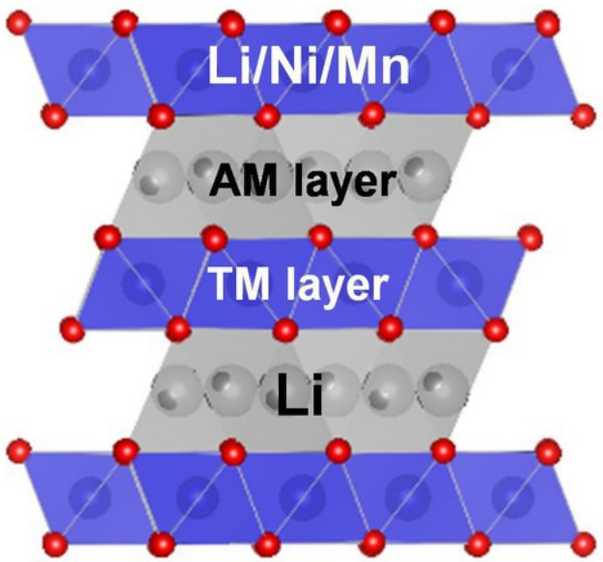

Tetrahedral site
(T-site)